Supporting information - A 310 nm optically pumped AlGaN vertical-cavity surface-emitting laser

Filip Hjort[1], Johannes Enslin[2], Munise Cobet[2], Michael A. Bergmann[1], Johan Gustavsson[1], Tim Kolbe[3], Arne Knauer[3], Felix Nippert[2], Ines Häusler[4], Markus R. Wagner[2], Tim Wernicke[2], Michael Kneissl[2], and Åsa Haglund[1]

[1] *Department of Microtechnology and Nanoscience, Chalmers University of Technology, 41296 Gothenburg, Sweden*
[2] *Institute of Solid State Physics, Technische Universität Berlin, 10623 Berlin, Germany*
[3] *Ferdinand-Braun-Institut, Leibniz-Institut für Höchstfrequenztechnik, 12489 Berlin, Germany*
[4] *Institute of Optics and Atomic Physics, Technische Universität Berlin, 10623 Berlin, Germany*

Pages S1 to S13
Figures S1 to S9

1 Dielectric DBR reflectivity

The simulated and experimentally measured reflectivity of the HfO_2/SiO_2 DBRs are shown in Fig. S1. As can be seen from Fig. S1a, the insertion of an Al layer below the bottom DBR increases the bottom DBR reflectivity at the 266 nm pump laser wavelength significantly compared to if only an Au bond metal would be used. Fig. S1b shows the simulated top DBR reflectivity on the $Al_{0.60}Ga_{0.40}N$ cavity layer while Fig. S1c,d shows the measured and simulated reflectivity for the same DBR deposited on a Si reference wafer. The measured peak reflectivity is above 99%. The blue shift of the stopband of less than 5 nm is due to minor thickness deviations originating from lateral variations in the chamber and a small drift in deposition rate during a run.

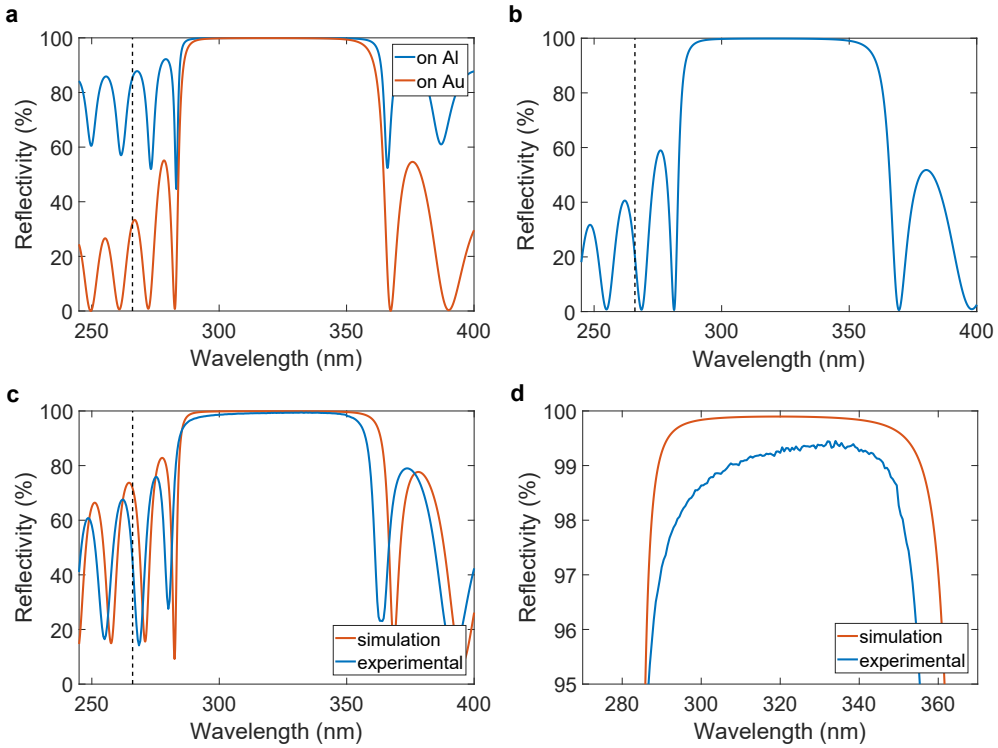

Figure S1: Reflectivity of the DBRs. **a**, Simulated bottom DBR reflectivity for the case where the DBR is terminated with an Al mirror and the case when terminated with Au. **b**, Simulated reflectivity for the top DBR on $Al_{0.60}Ga_{0.40}N$ and, **c**, simulated and measured reflectivity of the top DBR on Si. **d**, Magnified view of the stopbands in **c**. The dashed lines in **a**, **b**, and **c** mark the pump wavelength of 266 nm.

2 Estimation of threshold carrier density in QWs

To estimate the threshold carrier density in the QWs, an estimation of the fraction of the pump beam entering the cavity must first be made. As seen in Fig. S1b, the exact reflection at 266 nm is highly dependent on the spectral position of the DBR sidebands, which in turn depends on the precise DBR layer thicknesses and angle of incidence, adding a large deal of uncertainty to this estimation. Nevertheless, the reflection of the top DBR is estimated from the simulations to be in the 0-40% range. The next step is to make an approximation of the pump beam fraction that is absorbed in the cavity. At the pump wavelength of 266 nm, the absorption coefficient is assumed to be $1.5\times10^5\,\mathrm{cm}^{-1}$ for the QWs, $1.2\times10^5\,\mathrm{cm}^{-1}$ for the $Al_{0.50}Ga_{0.50}N$ in the barriers and the layers adjacent to the active region, and $1.6\times10^4\,\mathrm{cm}^{-1}$ for the $Al_{0.60}Ga_{0.40}N$ constituting the majority of the cavity.[1] However, it is important to note that the values of the absorption coefficients are sensitive to the exact Al-content and material quality, especially for $Al_{0.60}Ga_{0.40}N$ where the extent of band tailing has a large influence. Of the photons entering the AlGaN cavity, approximately 30% will be absorbed during the first pass through the top $Al_{0.60}Ga_{0.40}N$. Of the remaining intensity, almost 60% is absorbed while passing through the active region and surrounding $Al_{0.50}Ga_{0.50}N$ layers. The bottom $Al_{0.60}Ga_{0.40}N$ layer will absorb less than 10% of the pump beam. Thus, around 70% of the intensity entering the cavity will be absorbed during one pass. In addition, the bottom DBR is designed to reflect back a significant part of the pump beam, as illustrated in Fig. S1a, and this reflection is estimated to be in the interval 55-85%. Considering all the reflections and the absorption in the AlGaN, the fraction of the pump beam photons generating electron-hole pairs is estimated to be 70% ($\pm$ ~20%). Around 90% of the carriers are generated in the cavity outside of the QWs and intermediate barriers, but only a fraction of these are able to reach the active region. The fraction of the total amount of generated carriers reaching the QWs is assumed to be 50% ($\pm$ ~30%) but is hard to estimate as it depends on, for example, distance to the active region, material composition, defects, and recombination rate.

The pulse energy required from the 266-nm pump laser for the UVB VCSEL in Fig. 2 to reach threshold is 15 nJ. The pump laser has a pulse length of 1.3 ns and is focused to a spot size of approximately 12 µm in diameter. This thus corresponds to $13\,\mathrm{mJ/cm^2}$ and a pumping power density of $10\,\mathrm{MW/cm^2}$ during the pulse, assuming a square-shaped pump intensity distribution in both space and time. Areas with threshold power densities below $3\,\mathrm{MW/cm^2}$ were also measured. For a power density of for example 6 $\mathrm{MW/cm^2}$, the generation rate during the pulse in the three, 2 nm thick QWs is $5\times10^{30}\,\mathrm{cm^{-3}s^{-1}}$, assuming that 70% of the pump beam is absorbed in the cavity and that 50% of the generated carriers reach the active region. Knowing the generation rate, the carrier density is directly determined by the carrier lifetime. In similar QWs we have previously measured photoluminescence decay times of approximately 300 ps at room temperature.[2] As this is significantly shorter than the pump pulse width, it can be expected that the carrier density in the QWs during the pulse reaches a steady-state value. In addition, carrier lifetimes usually decrease significantly with increased pumping density[3] and the pumping densities are orders of magnitudes higher in this study than in our previous time-resolved photoluminescence measurements. Assuming a carrier lifetime of 100 ps around threshold, the threshold carrier density in the QWs for threshold power densities of $(6\pm4)\,\mathrm{MW/cm^2}$ becomes $(5\pm3)\times10^{20}\,\mathrm{cm^{-3}}$, or equivalent $(10\pm6)\times10^{13}\,\mathrm{cm^{-2}}$ per QW. These values are dependent on the numerous assumptions made and if the estimated uncertainty for the fraction of photons absorbed and number of carriers reaching the QWs is included, together with an estimated range of photoluminescence decay times of 30-300 ps, the calculated threshold carrier density range widens to 2×10^{19} - $5\times10^{21}\,\mathrm{cm^{-3}}$ for 2-10 $\mathrm{MW/cm^2}$ in threshold pump power density. As AlGaN QWs usually need carrier densities in the low $10^{19}\,\mathrm{cm^{-3}}$ to reach transparency[4], threshold QW carrier densities in the 10^{19}-$10^{21}\,\mathrm{cm^{-3}}$ range are reasonable considering that the UVB VCSELs demonstrated here have relatively large detuning between the cavity resonance wavelength and the photoluminescence peak wavelength and that optical losses might still leave room for improvement.

3 UVB VCSEL design and resonance wavelength

The refractive index and the simulated longitudinal optical field as function of vertical position in the AlGaN VCSEL are shown in Fig. S2. In order to achieve large modal gain, the cavity is designed to have an antinode at the position of the three QWs. The calculated threshold material gain in the QWs for this structure, which has a resonance at the design wavelength of 320 nm, is 1113 cm^{-1}. For a structure with identical DBRs but with a slightly shorter cavity length (defined as the distance between the DBRs) of 310.5 nm instead of 330.5 nm and a resonance wavelength of 309 nm, corresponding to the case presented in Fig. 2-4, the threshold material gain in the QWs is instead 1325 cm^{-1}.

Figure S3a shows the deviations in cavity length from the designed thickness of 330.5 nm that correspond to the wavelengths of the different longitudinal modes. The blue circles mark the wavelength of the mode with the lowest simulated threshold material gain in the QWs for a given cavity thickness deviation. Figure S3b displays the measured angle-resolved spectra below and above threshold for a VCSEL without the 10.4 nm HfO_2 detuning layer that was deposited before the top DBR for the VCSELs presented in the letter. In Fig. S3b, two clear angular-dispersive cavity modes can be seen, one around 305 nm (2.5λ cavity) and one close to 345 nm (2λ cavity). This corresponds to a cavity length that is approximately 25 nm shorter than designed. The 40 nm spacing between the 2.5λ and 2λ longitudinal modes agrees well with the simulation results in Fig. S3a. The shift in lasing wavelength from design can be due to a number of different factors. For example, a physical thickness deviation of as little as 10 nm would result in a shift of lasing wavelength of around 5 nm for this 2.5λ cavity, see Fig. S3a. In addition, the optical cavity length may also be affected by a different Al-content in the cavity compared to the intended content and slight deviations in refractive indexes between the actual values and those used in the simulations.

Figure S4 shows the variation in total optical intensity as well as spectral position of the 2λ peak in the spectrum below threshold for a VCSEL without the HfO_2 layer below the top DBR. The spatially resolved emission was measured in a back-scattering geometry through a 20x objective lens (NA=0.4), which was mounted on a piezo stage. The sample was excited with the fourth harmonic of a fiber laser with λ = 258 nm with a pulse length of 2 ps at 80 MHz repetition rate. The pulse energy at the sample surface amounts to approximately 1 mJ/cm^2. The collected signal was dispersed in a 0.75 m focal length monochromator equipped with a 150 l/mm grating and detected with a UV-enhanced Si–charge-coupled device array. The spectral resolution of the setup was 0.2 nm. In Fig. S4a, the shape of the region with high intensity corresponds to the shape of the Al mirror, demonstrating the increased mirror reflectivity by the Al. As can be seen from Fig. S4b,c, the spectral position of the 2λ mode around 340-345 nm can vary several nanometers over a few micrometer wide spatial region. As shown by the simulations, this can be caused by cavity thickness variations of a few nanometers, which would result in similar wavelength shifts for the 2.5λ as for the 2λ mode. The results thus explain why there is simultaneous lasing at multiple wavelengths between 305 nm and 310 nm at several laterally confined positions when pumping with a 12 µm pump spot for the angle-resolved PL measurements.

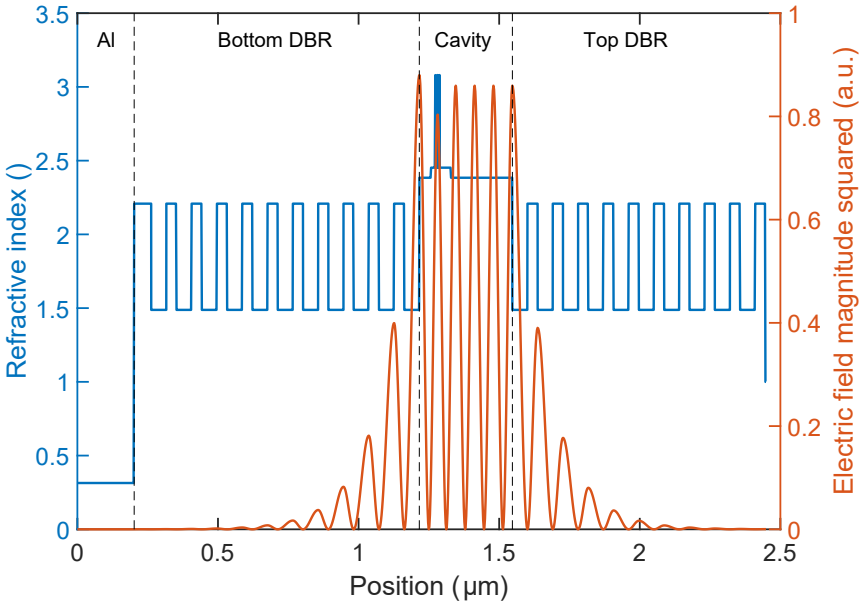

Figure S2: UVB VCSEL structure and optical field profile. Refractive index and magnitude squared of the electric field as a function of the vertical position in the 2.5λ cavity.

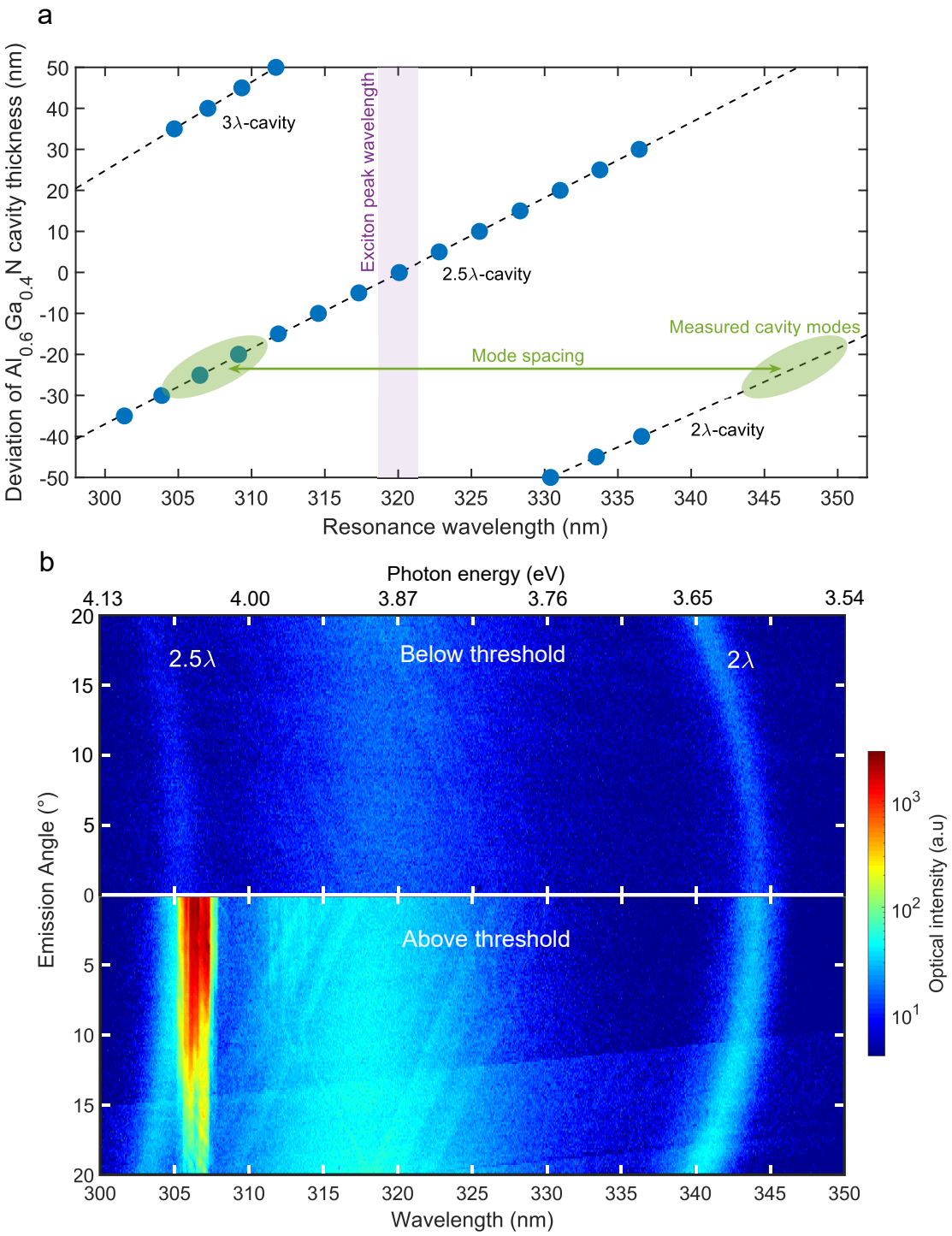

Figure S3: Longitudinal modes in the UVB VCSEL cavity. **a**, Resonance wavelength (dashed lines) of different longitudinal modes and the corresponding thickness deviation of the $Al_{0.60}Ga_{0.40}N$ cavity layers. The blue circles mark the resonance wavelength with lowest QW threshold gain for a given cavity thickness deviation and the green ellipses indicate the measured cavity modes. **b**, Angle-resolved emission spectra of a VCSEL without the HfO_2 detuning layer. The top is below threshold and the bottom part is above threshold and the angular-dispersive 2.5λ and 2λ modes are marked in the figure.

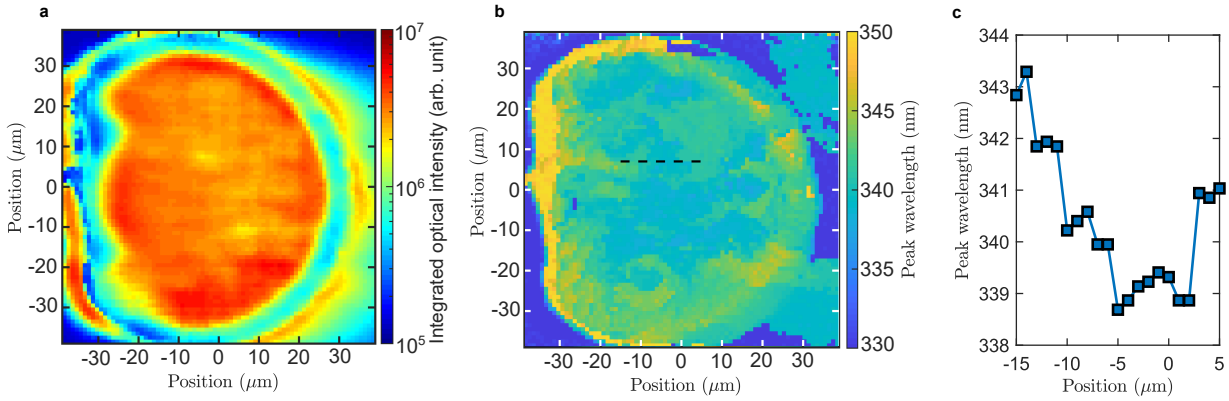

Figure S4: Spatial variation of resonance wavelength a, Spatial variation of the micro-PL integrated optical intensity from 270 nm to 360 nm below threshold for a VCSEL without the extra HfO_2 layer below the top DBR. The mesa is similarly shaped as the mesa imaged in Fig. S7o but with smaller diameter. **b**, Spatial variation of the peak wavelength in the spectral range from 330 nm to 350 nm. **c**, Peak wavelength versus position along the black dashed line marked in **b**.

4 Strain state of the UVB VCSEL heterostructure

Low threading dislocation densities in the active region are needed to ensure low threshold pump power densities. This is particularly challenging for devices emitting in the UVB spectral region due to the large lateral lattice mismatch between the used AlN on sapphire template and the active region with Al-contents as low as $x = 0.2$.

Since relaxation is unavoidable, it is important to initiate the relaxation process a large distance away from the active region. In order to realize a controlled strain relaxation and relatively smooth surface morphology, an AlN/GaN-superlattice, similar to Ref. [5], and graded AlGaN layers are grown on top of the AlN on sapphire template. Using a high resolution X-ray diffraction (HRXRD) reciprocal space map (RSM) of the asymmetric $(10\bar{1}5)$ reflection near AlN, it is not only possible to investigate the composition of the grown layers, but also to get insight into the strain state of the heterostructure. The asymmetric RSM was recorded using an X'Pert Pro MRD with a hybrid monochromator and a 2D-array detector and is shown in Fig. S5. Diagonal solid grey lines illustrate the position of reflections of an AlGaN layer of distinct composition but varying strain. Furthermore, the position of the reflection of relaxed AlGaN layers with different composition is plotted between AlN and GaN. The AlN layer and the superlattice reflections are visible in the RSM around Q_x-values of $2.33\,\text{Å}^{-1}$ and Q_z-values of $6.30\,\text{Å}^{-1}$. The first part of the subsequently grown pseudosubstrate shows intensity at a position close to the vertical black line indicating that the layer is pseudomorphically strained to AlN with an Al-content of $x = 0.71$. After that a broad relaxation gradient (shift along grey lines) as well as a change in Al-content (shift along AlN-GaN-line) is visible. This relaxation and compositional shift results in a lattice constant of the layer which is close to the one of relaxed $Al_{0.55}Ga_{0.45}N$. Previous investigations showed that the relaxation process is not assisted by the formation of new structural defects, but by bending of already existing threading dislocations.[5,6] This process leads to a defect density of around $2 \times 10^9\,\text{cm}^{-2}$.[6] The lateral lattice constant achieved by this pseudosubstrate acts as basis for further heterostructure growth.

Figure S5 shows that the further heterostructure growth does not lead to major relaxation within the structure (same Q_x-value as pseudosubstrate, black dotted line). The sacrificial layer as well as the sacrificial superlattice which are essential for the etching process can be identified at Q_z-values between $6.08\,\text{Å}^{-1}$ and $6.15\,\text{Å}^{-1}$. Furthermore, the upper and lower cavity layers are visible in the RSM at a similar Q_x-value as the underlying layers with no strong indication of relaxation or peak broadening, which could indicate a lower layer quality. Using this approach, fully strained sacrificial layers were achieved as well as the growth of a VCSEL structure without the introduction of new defects within the active region.

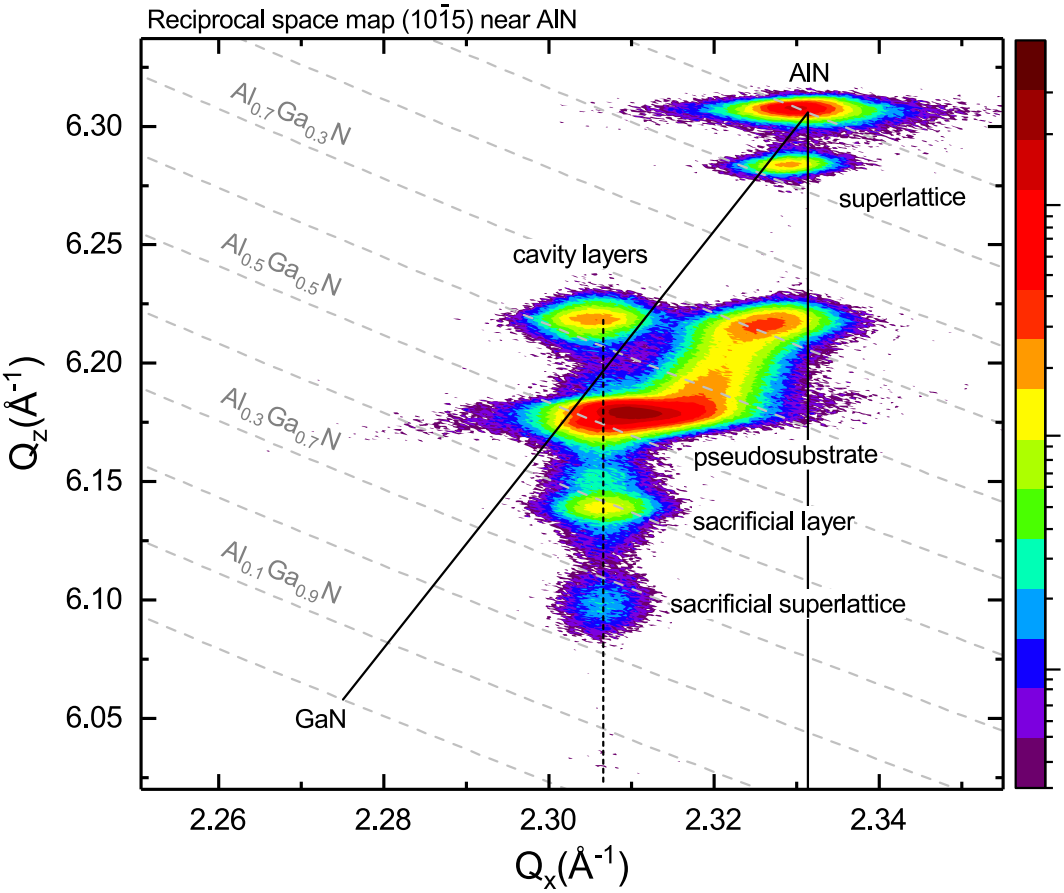

Figure S5: Strain state of epitaxial heterostructure. X-ray diffraction reciprocal space map near the (10$\bar{1}$5) reflection of AlN illustrating the relaxed pseudosubstrate, the sacrificial layer as well as the strained cavity layers on top of the heterostructure.

5 Structural analysis of the UVB VCSEL heterostructure

In order to prove the structural quality as well as the precise control of the layer thicknesses of the epitaxial structure, an as-grown VCSEL structure with a cavity length of 1.5λ was investigated using transmission electron microscopy (TEM). A FEI Titan 80-300 TEM equipped with an image Cs-corrector was used. All TEM images were recorded with an acceleration voltage of 300 kV. Figure S6a shows an overview image of the as-grown VCSEL structure with the bottom cavity layer, the first barrier, active region, last barrier, and top cavity layer. The top and bottom cavity layers show a deviation of only 2% from the intended thicknesses. The zoomed in high resolution TEM image in Fig. S6b reveals the structure and thickness of the active region. The quality of the QWs is high, with sharp interfaces between QWs and barriers, laterally homogeneous QW thickness and same thickness of all QWs.

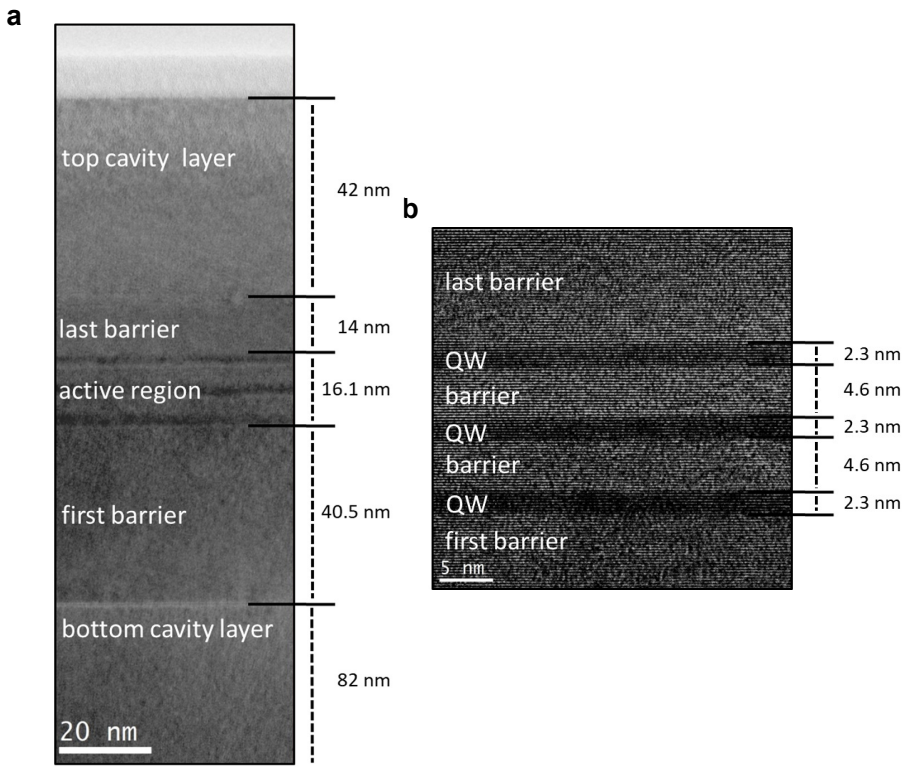

Figure S6: TEM investigation. a, Overview TEM image of an as-grown 1.5λ-cavity UVB VCSEL structure and, **b**, high resolution TEM image of the active region.

6 UVB VCSEL process flow

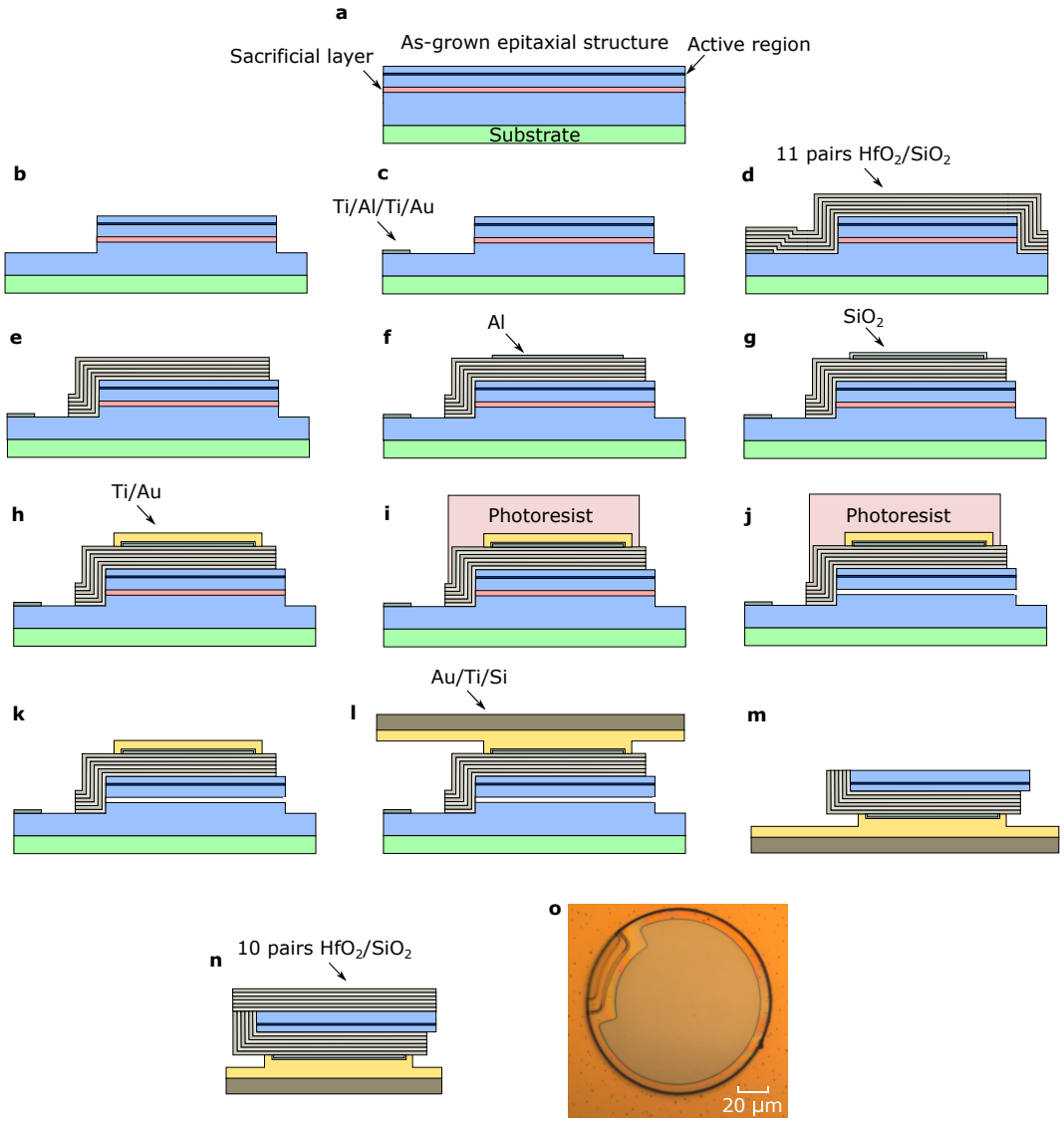

Figure S7: Process flow and optical microscope image.. Schematic cross section of the sample, **a**, before processing, **b**, after mesa dry etching, **c**, after evaporation of electrochemical etch contact, **d**, after first DBR deposition, **e**, after DBR dry etching, **f**, after Al evaporation, **g**, after SiO_2 sputtering, **h**, after Ti/Au evaporation, **i**, after photoresist protection, **j**, after electrochemical etching, **k**, after photoresist removal, **l**, during thermocompression bonding, **m**, after thermocompression bonding, and, **n**, after the second DBR deposition, forming the final UVB VCSEL device. **o**, Top-view optical microscope image of the fabricated UVB VCSEL after the final processing step.

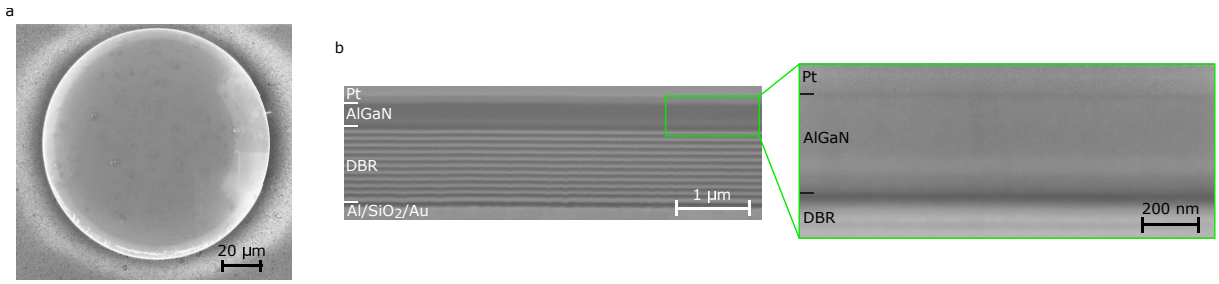

Figure S8: SEM images of the sample before top DBR deposition. a, Top-view SEM image and, **b**, cross-sectional SEM image of the sample before top DBR deposition. The Pt in **b** is deposited to protect the top surface during the focused ion beam milling used to expose the device layers seen in the cross-sectional view.

7 UVB VCSEL photoluminescence measurements

The in-plane momentum $k_{||}$ of resonant photons in a planar microcavity is directly related to the external angle q of the emission in the far field via the relation $k_{||} = (E/\hbar c)\sin(q)$. This enables recording the dispersion in k-space directly using angle-resolved micro-photoluminescence. It can therefore be used to distinguish between the longitudinal modes that are dispersive in k-space (and hence angular-dispersive) and non-dispersive excitonic emission. The angle-resolved micro-photoluminescence setup used is described in Fig. S9. It is additionally used to determine lasing threshold pump power, laser beam divergence, polarization, and linewidth of the emission. An additional feature of the setup is imaging the spatial emission distribution at the sample surface and thus allowing an evaluation of the spatial properties of the lasing output such as filamentation and inhomogeneity due to structural or compositional disorder.

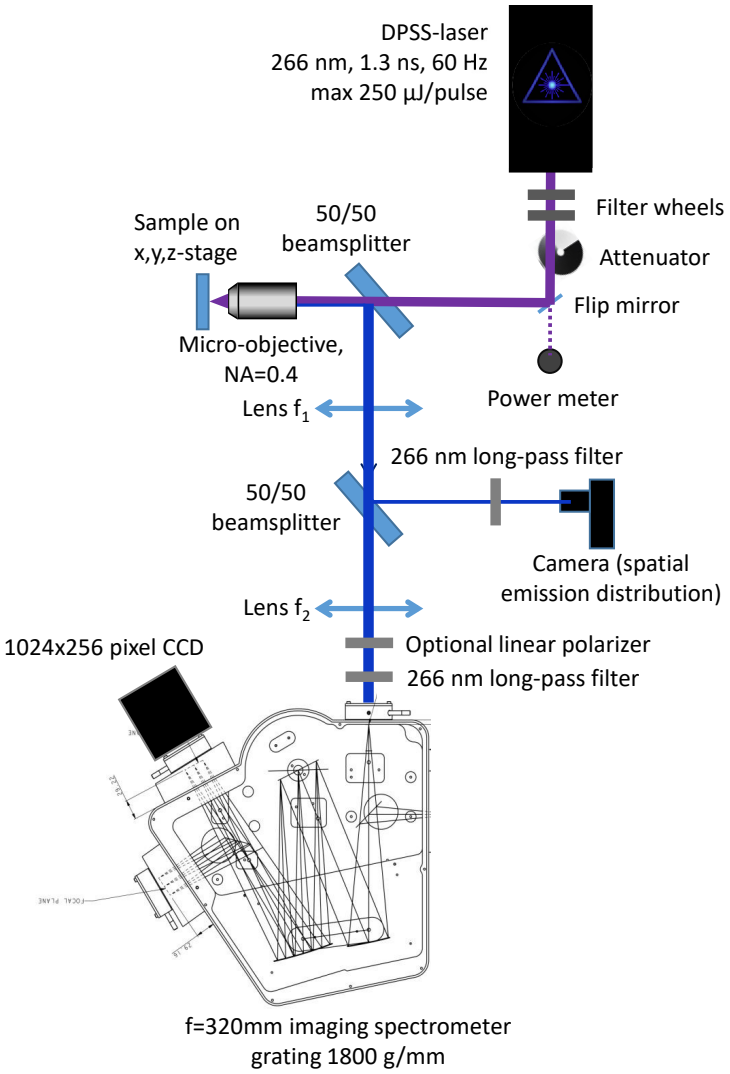

Figure S9: Photoluminescence measurement setup. Setup to measure angle-resolved spectrum, spatial emission distribution at the sample surface, polarization of the UVB VCSEL output emission. Excitation is done with a pulsed diode-pumped solid-state (DPSS) laser.

References

1. Winkler, M. *et al. Anisotropic dispersion model of AlGaN.* Otto von Guericke University Magdeburg, unpublished raw data.
2. Bergmann, M. A. *et al.* Electrochemical etching of AlGaN for the realization of thin-film devices. *Appl. Phys. Lett.* **115,** 182103 (2019).
3. Nippert, F. *et al.* Auger recombination in AlGaN quantum wells for UV light-emitting diodes. *Appl. Phys. Lett.* **113,** 071107 (2018).
4. Chow, W. W. & Kneissl, M. Laser gain properties of AlGaN quantum wells. *J. Appl. Phys.* **98,** 114502 (2005).
5. Enslin, J. *et al.* Metamorphic $Al_{0.5}Ga_{0.5}N$:Si on AlN/sapphire for the growth of UVB LEDs. *J. Cryst. Growth* **464,** 185–189 (2017).
6. Mogilatenko, A. *et al.* V-pit to truncated pyramid transition in AlGaN-based heterostructures. *Semicond. Sci. Technol.* **30,** 114010 (2015).